RSC Advances

PAPER

View Article Online
View Journal | View Issue

Cite this: *RSC Adv.*, 2020, **10**, 30944

A coupled model of electromagnetic and heat on nanosecond-laser ablation of impurity-containing aluminum alloy

Jiaheng Yin, Yongzhi Cao,* Yongda Yan, Lihua Lu, Jiaxuan Chen and Fuli Yu

Received 29th May 2020
Accepted 29th July 2020

DOI: 10.1039/d0ra04730a

rsc.li/rsc-advances

In the emerging field of laser-driven inertial confinement fusion, Joule heating generated *via* electromagnetic heating of the metal frame is a critical issue. However, there are few reported models explaining thermal damage to the aluminum alloy. The aim of this study was to build a coupled model for electromagnetic radiation and heat conversion of an ultrashort laser pulse on an aluminum alloy based on Ohm's law. Additionally, the application SiO_2 films on aluminum alloy to improve the laser-induced damage threshold (LIDT) were simulated, and the effects of metal impurities in the aluminum alloy were analyzed. A model examining the relation between electromagnetic radiation and heat for a nanosecond laser irradiating an aluminum alloy was developed using a coupled model equation. The results obtained using the finite difference time domain (FDTD) algorithm can provide a theoretical basis for future improvement of the aluminum alloy LIDT.

1. Introduction

Laser-driven inertial confinement fusion (ICF) can generate large amounts of renewable energy *via* the chemical reaction of two forms of hydrogen—deuterium (D) and tritium (T)[1]—and the reaction is expressed in eqn (1). However, the half-life of tritium (T) is short and it does not occur naturally; furthermore, it is extremely difficult to obtain *via* reaction. Hence, tritium in fusion reactors needs to be recycled, using doubled neutrons for reaction with lithium followed by recovery of tritium, where tritium functions like a catalyst (reaction shown in eqn (2)).[2] Because of its potential advantages for quickly generating a large, inexhaustible amount of clean energy.[3–5] A nuclear laser facility can reach 1.8 MJ and 500 TW of 355 nm light in 10^{-9} s, which is equivalent to 1000 times the energy consumption of the United States.[6] The French Megajoule Laser Project (LMJ) supported by the French Atomic Energy Commission (CEA)[7] and the American National Ignition Facility Project (NIF) are collaborating with Lawrence Berkeley National Laboratory[8] to realize this goal. For this process, damage to optical elements such as fused silica and potassium dihydrogen phosphate (KDP) is an important topic of research.[9,10] However, laser-induced damage of the aluminum alloy frame for the entire system has not been comprehensively studied, especially *via* theoretical research.

$$^{2}_{1}\mathrm{D} + ^{3}_{1}\mathrm{T} \rightarrow ^{4}_{2}\mathrm{He}\ (3.5\ \mathrm{MeV}) + ^{0}\mathrm{n}\ (14.1\ \mathrm{MeV}) \quad (1)$$

$$^{0}\mathrm{n} + ^{6}_{3}\mathrm{Li} \rightarrow ^{3}_{1}\mathrm{T} + ^{4}_{2}\mathrm{He} + 4.784\ \mathrm{MeV} \quad (2)$$

The traditional laser power conversion configuration is usually applied to photovoltaic (PV) cells. Light-to-heat generation and light-to-electricity conversion have recently seen research progress.[11,12] Previous work aimed at improving the efficiency between the input power and the power output by the battery, and some studies attributed the low ceiling to the temperature.[13,14] While laser-induced damage in dielectrics is related to the pulse duration, there are qualitative differences between multi-photon ionization and Joule heating, which include plasma formation and conventional melting.[15] The energy coupling mechanism between an ultrashort pulse laser and optical materials has become an issue of intense research interest, including the exploration of surface damage initiation,[16] the optical breakdown process,[17] electronic excitation–relaxation processes,[18] and particle generation.[19] Studies have been limited to either experimental or single-simulation investigation of the influence of the pulse duration,[20] laser fluence, and wavelength[21] on site damage or the morphology of the optical elements. The impact of the electric-field distribution on field enhancement was simulated[22] and a temperature model was established to analyze the interaction between the laser and metallic materials.[23] To investigate impurities present in the crystals, Bhar *et al.* studied the LIDT and the effect of inclusions in some nonlinear crystals; they found that Na^+ ion inclusion and the LIDT of the BBO crystals were correlated.[24] Some studies investigated the laser-induced damage threshold (LIDT) of the TiO_2/SiO_2 multilayer reflective coatings and determined the ultra-short LIDT of KH_2PO_4 *via* simulation. They studied the effects of lasers of different wavelengths on the optical

Center for Precision Engineering, Harbin Institute of Technology, Harbin, 150001, China. E-mail: cflying@hit.edu.cn; Fax: +86-451-86415244; Tel: +86-451-86412924

properties of dielectric materials experimentally and *via* simulations.[25,26] This research was aimed at studying the laser damage threshold, the reflectivity curve of a TiO_2 single-layer film (experimentally and fitted), and the GIXRD of SiO_2 and TiO_2 single layers. However, the relationship between the laser fluence and the temperature was not investigated in detail. Hence, the search for a coupled model for electromagnetic radiation and heat conversion during nanosecond-laser ablation of aluminum alloy is still an unresolved issue.

Moreover, energy conversion resulting in laser-induced damage of a thin film has not been widely studied, and other aspects of thin films used for PV cells have generally received more attention. For example, the double-pulse temporal method was applied to a thin foil film, the results showed that the energy conversion efficiency was 15% higher than with a single pulse,[27] and Cu_2ZnSnS_4 thin films are widely applied in solar cells. These studies focused more on pulsed laser film deposition,[28] energy conversion efficiency,[29] and the fabrication of thin films.[30] Silica is used in optical elements because of its antireflection properties in high-power laser systems, which can improve the LIDT of the optical components.[31,32] Studies have mostly been confined to the laser parameters, including the pulse duration,[33] laser fluence,[34] and wavelength,[35] as well as to the film processing parameters including the thickness and organic groups[36] that affect the growth of the silica thin film, such as its morphology and growth rate. However, studies have not modeled the relation between electromagnetic radiation and heat in the silicon dioxide thin films. Therefore, a coupled model that is related to the aluminum alloy and the silicon dioxide thin film used as a surface coating needs to be investigated; this should extend beyond the relation between electromagnetic radiation and heat and also include the silicon dioxide film and its substrate.

In this work, a coupled model was built for electromagnetic radiation and heat conversion in an aluminum alloy with a nanosecond-laser. We first investigated the effect of copper impurities at a certain depth in the aluminum alloy under UV laser irradiation *via* FDTD simulations. Then, the light-to-electricity conversion was studied. The results of the light intensity enhancement factor (LIEF) of the aluminum alloy before and after coating with the SiO_2 thin films were determined. Finally, the effect of metal impurities (copper and aluminum) in the aluminum alloy on the temperature rise was simulated and the conclusions are outlined.

2. Coupled geometric modeling of electromagnetic and heat

The coupled model of electromagnetic radiation and heat was based on Ohm's law. Electromagnetic radiation to heat conversion in the structure can be assigned to the response to ohmic loss and Joule heating. The power dissipated is equivalent to:

$$P = \boldsymbol{J} \times \boldsymbol{E}, \tag{3}$$

where $\boldsymbol{J}$ is the current density and $\boldsymbol{E}$ is the electric field. When the equation was applied to the coupled model of electromagnetic and heat conversion, the applied heat energy transfer rate (W m^{-3}) is $Q = P$. According to research about the metal,[37,38] the heat transport equation can be expressed as follows:

$$Q = \varepsilon\omega_0 \mathrm{Im}|\boldsymbol{E}(r)|^2, \tag{4}$$

where ω_0 is the angular frequency and ε is the permittivity of the metal. This equation shows the relationship between the incident electric field and the imaginary part of the permittivity. Generally, metal particles like Cu and Al are usually located at a certain depth in the alloy or film. However, the difference between plasma formation, ablation, and conventional heating of materials depends on the duration of laser action.[15] In this case, two processes were responsible for the laser-induced damage of the material. The damage was first due to ablation by high-power laser-induced multiphoton ionization, and then heat conduction and thermal explosion based on absorption by the impurities occurs. The surrounding metal particles are in contact with the air after the first step, and then the ultrashort pulse laser acts as a heat source and leads to a rise in temperature. The power dissipated can be equivalent to $P = \sigma E^2$, where σ is the electrical conductivity of the metal. According to Maxwell's equations, the relationship between the magnetic field $\boldsymbol{H}$ and the current density $\boldsymbol{J}$ can be expressed based on Ampere's law:

$$\oint \boldsymbol{H} \times \mathrm{d}l = \int \boldsymbol{J} \times \mathrm{d}s. \tag{5}$$

This indicates that the line integral of the magnetic field along any loop is equal to the current intensity in any curved surface with the loop as the boundary. The linear relationship between the magnetic field $\boldsymbol{H}$ and the current density $\boldsymbol{J}$ shows that the heat energy transfer rate Q has a quadratic relationship with the rotational magnetic field $\boldsymbol{H}_0$. Eqn (3) indicates that the heat energy transfer rate of the metal particles is related to the magnetic field, which provides us with an approach to decrease the magnetic field around the metal particles and reduce the ohmic loss.

The calculation flow chart for the coupled model of electromagnetic radiation and heat on nanosecond-laser ablation is presented in Fig. 1. The steps to simulate the electromagnetic radiation to heat conversion using the coupled model is as follows:

- Step 1: after irradiation with a high-fluence nanosecond laser, the electromagnetic field was first calculated until the field reached a steady-state inside the object.
- Step 2: the power, which dissipated because of ohmic loss, was next calculated based on eqn (3), which was then applied to the heat transport equations as the heat energy transfer rate.
- Step 3: once the desired simulation time was reached, the simulation was stopped.

Fig. 2 shows the process used to obtain the coupled model for the electromagnetic field and heat during nanosecond laser ablation. It can be seen from Fig. 2(a) and (b) that the thickness of the aluminum alloy for its own micro arc oxide layer and after coating with a silicon dioxide thin film remains consistent

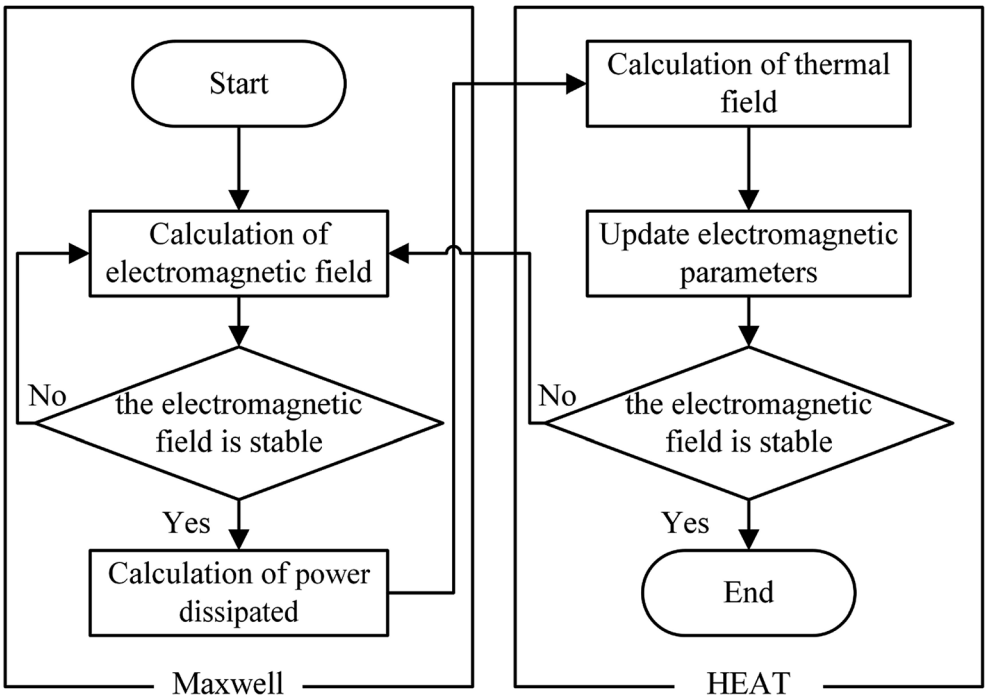

Fig. 1 Flow chart for the electromagnetic and heat coupling analysis.

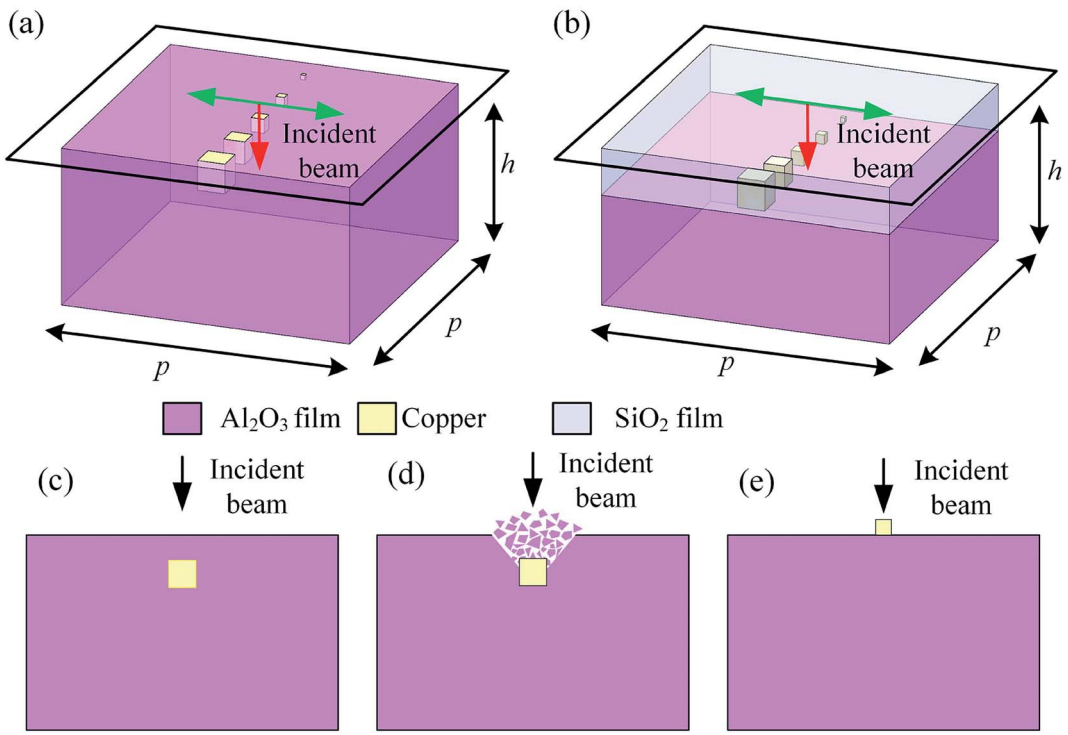

Fig. 2 Process diagram for the thin-film electromagnetic field and heat coupling damage under laser irradiation. (a) Metal particles underneath the micro arc oxide layer (Al_2O_3 film). (b) Metal particles under the micro arc oxide layer (Al_2O_3 film) and silicon dioxide films (SiO_2 film). Both (a) and (b) with dimensions: $p = 20$ μm, $h = 10$ μm. (c) Irradiation begins. (d) Multiphoton ionization damage of the thin films. (e) Metal particles exposed to air and Joule heating.

($h = 10$ μm). Fig. 2(c)–(e) show the laser-induced damage process for the thin films doped with metal particles. The plasma formation and ablation first happened as shown in Fig. 2(a), and then the metal particles were exposed to air; for an irradiation time > 100 ps, both the particles and substrate were subject to conventional melting and boiling, as seen from

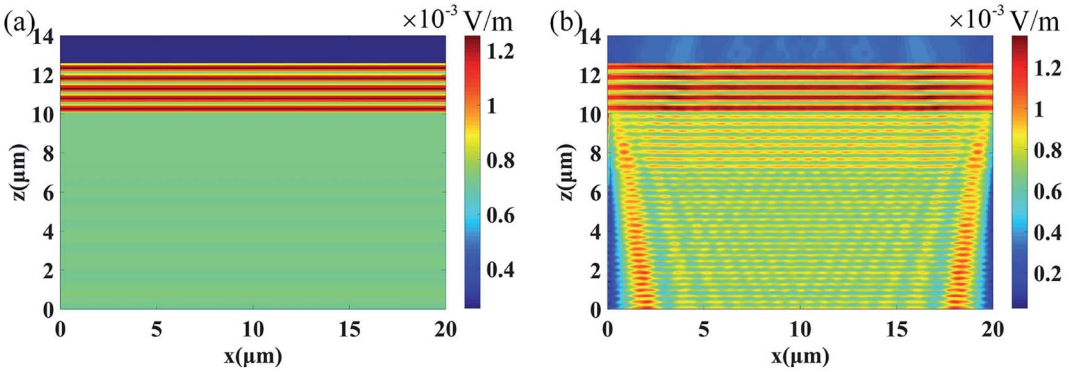

Fig. 3 FDTD simulation results for the TE mode E distribution at a normal incidence for non-metal doped (a) Al_2O_3 and (b) SiO_2 thin films.

Fig. 2(b). Because the temperature rise of the metal particles was faster, the temperature changes of the metal particles were primarily simulated after being exposed to air (see Fig. 2(c)).

3. Discussion and numerical simulation

3.1 Spectral characteristics of Al_2O_3 before and after coating with a SiO_2 thin film

The electric-field intensity in Al_2O_3 before and after coating with a silicon thin film was simulated using the FDTD method. To ensure accurate results for the simulation, the simulation domain was gridded with spacings at 12 samples per wavelength according to the Courant stability condition. Furthermore, to ensure uniformity of film thickness for each layer, the x- and y-directions adopted periodic boundary conditions while the z-direction adopted a perfectly matched layer-absorbing boundary condition.

The spectral characteristics took the form of a plane wave as the initial condition and the incident direction was in the z-direction at a normal incidence of 1.064 μm. According to the Fresnel reflection theory, a formula for calculating the transmission coefficient of the TE mode material at normal incidence can be expressed as follows.

$$r = \frac{E_t}{E_0} = \frac{2n_1}{n_1 + n_2}, \tag{6}$$

where r is the transmission coefficient and n_1 and n_2 are the refractive index of air and the material, respectively. The refractive indices at 1.064 μm for Al_2O_3 and SiO_2 are 1.754 and 1.453, respectively. The $\boldsymbol{E}_t$ of the transmission wave for Al_2O_3 and SiO_2 was 0.726 V m^{-1} and 0.815 V m^{-1}, respectively, while $\boldsymbol{E}_0$ was the normalized electric field. Based on eqn (5), the internal light intensity of Al_2O_3 and SiO_2 under nanosecond-laser irradiation was calculated, which were 1.2277 × 10^{-3} W m^{-2} and 1.2809 × 10^{-3} W m^{-2}, respectively.

$$I = \left|\frac{1}{T}\int_0^T S\mathrm{d}t\right| = \frac{1}{2}\sqrt{\frac{\varepsilon}{\mu}}|E|^2, \tag{7}$$

where I is the light intensity value, S is the Poynting vector, ε is the dielectric constant of the medium, and μ is the magnetic permeability of the medium. Fig. 3 demonstrates the FDTD numerical simulation results for the internal electric field intensity in Al_2O_3 before and after being coated by the thin film, and the amplitudes of the electric field intensity were 0.721 V m^{-1} and 0.812 V m^{-1}, respectively, and their internal light intensities were 1.2108 × 10^{-3} W m^{-2} and 1.2714 × 10^{-3} W m^{-2}, respectively. The relative error was within 2%, which means that the fit of the simulation results was in good agreement with the Fresnel theory. Hence, this method could be used to simulate the light intensity (I) well.

Fig. 4 shows the light intensity distributions for the Al_2O_3 thin films before and after coating with the SiO_2 thin films with mental copper cube particles of edge lengths 0.3, 0.6, 0.9, 1.4, and 1.9 μm. The differences in the light intensity distributions with the SiO_2 thin film coatings were not remarkable. The light intensity enhancement factor (LIEF) is widely applied to characterize the intensity enhancement of an aluminum alloy before and after coating by thin films with metal particles:

$$\mathrm{LIEFs} = \frac{I_{\max}}{I_0}, \tag{8}$$

where $I_{\max}$ is the maximum light intensity of the metal particle doped film and I_0 is the light intensity of non-metal particle doped film. The LIEFs of the Al_2O_3 thin films and SiO_2 thin films are listed in Table 1, as calculated using Fig. 4. The LIEFs of the SiO_2 thin films were ~50% and 25% those of the Al_2O_3 thin films when the edge length of the copper cubes were 0.3 and 0.6 μm, respectively. When the edge lengths of the cubes were 0.9 and 1.9 μm, the LIEFs of the SiO_2 thin films were ~85.9% and 78.4% of those of Al_2O_3 thin films. It is worth noting that the LIEFs of the 1.4 μm-edge length cube were almost the same. However, in general, after being coated by the SiO_2 thin films, the LIEFs were sharply reduced.

Differences in the LIEFs between the Al_2O_3 thin films and SiO_2 thin films could be attributed to the different types chemical bonds in the two materials. Photo-ionization and impact ionization led to an increase in the free electron density, which destroyed the metal frame because of the interaction between the strong laser field and the dielectric materials. SiO_2 is an atomic crystal, here, a Si atom forms four covalent bonds with four O atoms, while one oxygen atom

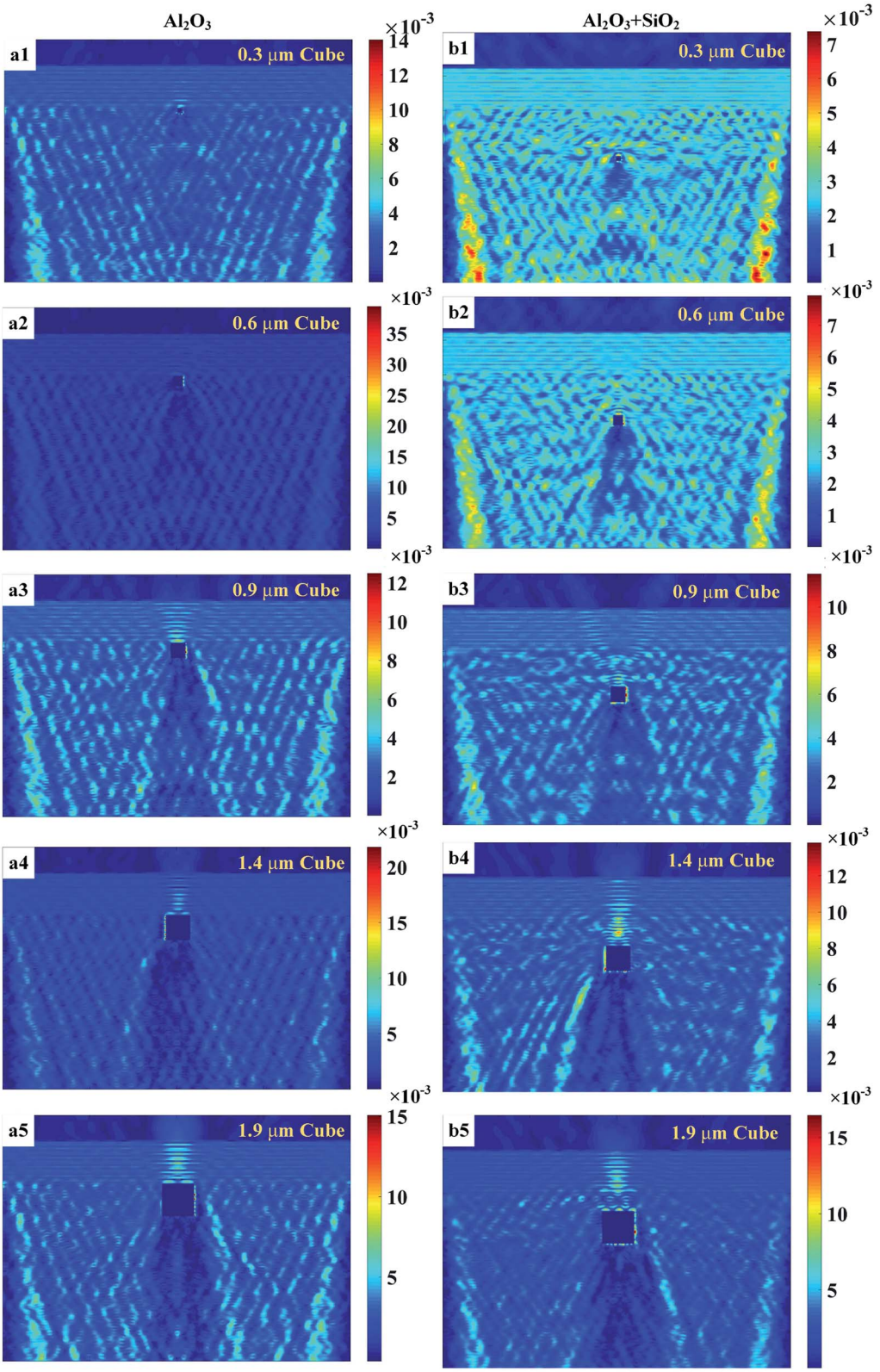

Fig. 4 FDTD simulation results for the TE mode light intensity distribution at $y = 0$, x–z plane: Al_2O_3 before (a1–a5) and after (b1–b5) being coated by SiO_2 thin films that are both doped with copper cubes of different edge lengths.

forms two covalent bonds with two Si atoms. The covalent bond is a type of chemical bond, here, two or more atoms use their outer electrons to reach a state of electronic saturation under ideal circumstances. This makes for a relatively stable chemical structure. The valence bond is the interaction between atoms *via* the sharing of electron pairs. The ionic

Table 1 LIEFs of Al_2O_3 before and after coating with the SiO_2 thin films

	Al_2O_3		SiO_2	
Cube (μm)	E (V m^{-1})	LIEFs	E (V m^{-1})	LIEFs
0.3	1.9	6.9	1.5	3.4
0.6	3.0	17.3	1.6, 6.6	3.9
0.9	2.1	8.5	2.2	7.3
1.4	2.0	7.7	2.3	7.8
1.9	2.4	11.1	2.4	8.7

bond refers to a chemical bond between anions and cations formed *via* electrostatic interaction, which occurs after two or more atoms or chemical groups lose or gain electrons and become ions. An electrostatic interaction is present between oppositely charged ions. When two oppositely charged ions are close, they are attracted to each other; there is mutual electrostatic repulsion between electrons and electrons and the nuclei and nuclei, when the electrostatic attraction and repulsion reach an equilibrium, ionic bonds are formed. The melting and boiling points of the SiO_2 atomic crystal are higher than those of Al_2O_3, which is an ionic crystal. This can explain the larger LIEF observed for the Al_2O_3 thin films than for the SiO_2 thin films.

3.2 Electromagnetic radiation and heat model for impurities-containing Al_2O_3

Fig. 5 shows the electromagnetic and heat model of Al_2O_3. For the structure in Fig. 5, the copper cube dimensions were 90 nm, and the Al_2O_3 substrate 20 μm × 20 μm × 10 μm was held at a laser fluence of $\Phi = 8$ J cm^{-2} with a laser wavelength of 1064 nm. We first ran the simulation and visualized the absorbed power density profile (shown in Fig. 5(a)), and then the absorption data were loaded in the heat source. Once the simulation was carried out, the results were loaded in the HEAT solver region and the temperature was visualized in Fig. 5(b) and (c). The result of the coupled electromagnetic and heat model showed that the highest temperature for copper was 1520 K, which was above the melting point (1357.77 K) and led to damage of the material (see Fig. 5(c)).

To investigate the effect of impurities on the temperature rise under different laser fluences (Φ), copper and aluminum cubes were placed in the Al_2O_3 substrate, with cube edge lengths between 50 and 90 nm in 10 nm intervals. The temperature rise curves are shown in Fig. 6(a) and (b), where the temperature rise (T) *vs.* laser fluence (Φ) is plotted. We can see that the temperature increased linearly with the laser fluence, as follows:

$$T = k\Phi + b, \tag{9}$$

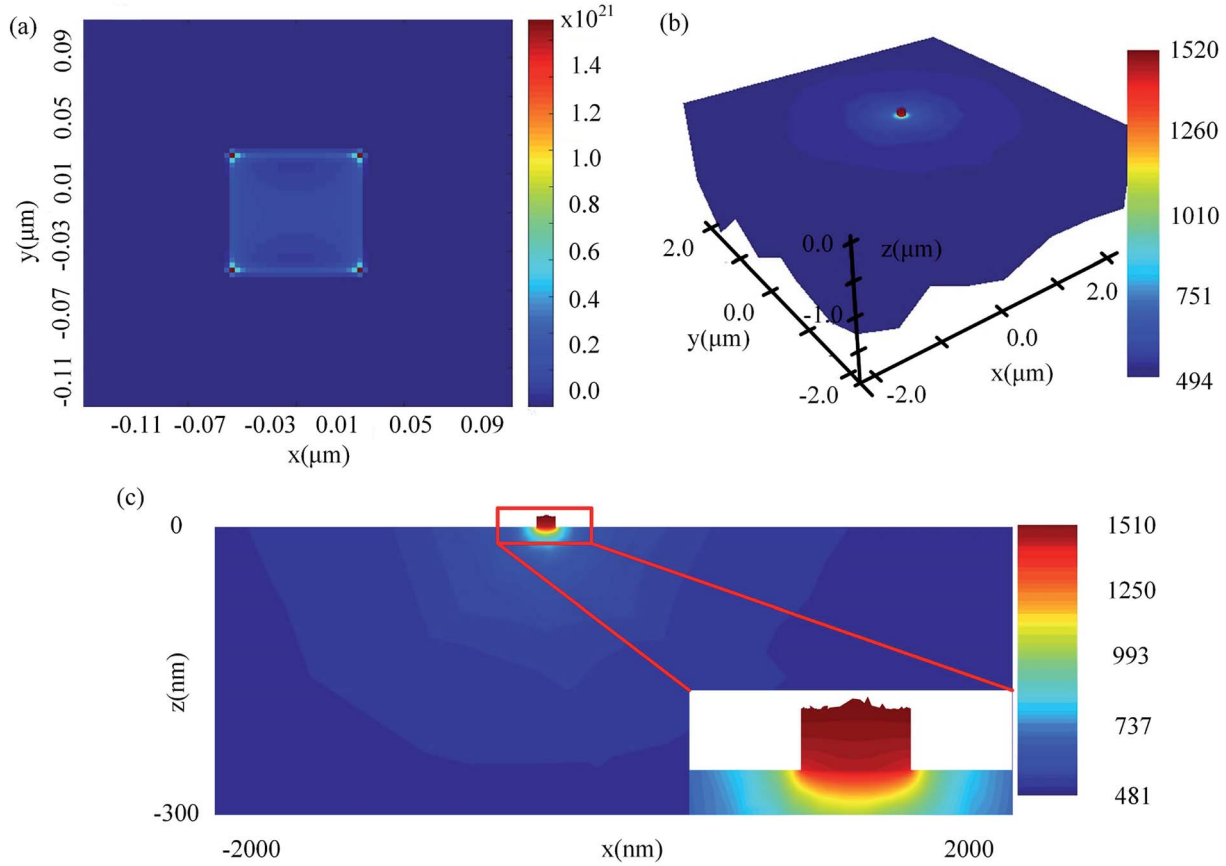

Fig. 5 (a) The absorbed power density profile. (b) Temperature profile at the copper and the top surface of the substrate. (c) Temperature profile underneath the superstructure at the center region, taken in the x–z plane (local magnification images on the lower right hand).

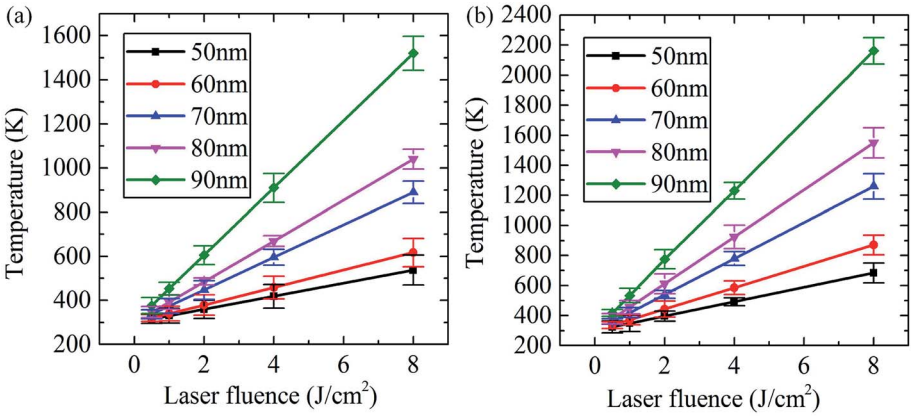

Fig. 6 Temperature rises along with increasing laser fluence and edge length of (a) copper and (b) aluminum.

Table 2 Comparison of simulation data for copper and aluminum impurities

	Copper			Aluminum		
Cube (nm)	k	b (K)	R^2	k	b (K)	R^2
50	29.61	300.21	0.99	48	300	1
60	39.59	300.08	0.99	71.35	300	0.99
70	73.74	300.00	0.99	120	300	1
80	92.52	299.58	0.99	156.26	299.58	1
90	152.49	300.08	1	232.09	303.7	0.99

where k is the proportionality growth coefficient and b is a constant, and Table 2 indicates the specific values for the copper and aluminum cubes under laser irradiation. R^2 is the coefficients of determination, and the data obtained for the two materials are shown to correspond well ($R^2 \geq 0.99$).

Table 2 shows that the temperature growth coefficient (k) increased with increasing cube size. The temperature growth coefficient for the copper cubes was smaller than for aluminum cubes, with the former being approximately two-thirds of the latter. Furthermore, the growth rate of the growth coefficient (k) increased a lot with increasing cube edge length. For a copper cube with a side length of 50 nm, the k was 29.61, and the k went up to 152.49 for a length of 90 nm, which is ~5 times larger. A similar trend was also observed for the aluminum cubes. Both of their constants (b) were ~300 K, and the results fit extremely well.

Fig. 6 intuitively compares the temperature (T) growth calculated using Lumerical's DGTD solver. The linear fit shown on the plot indicates that the 60 nm-length aluminum-cube almost reached its melting point (933.16 K) at a laser fluence (Φ) of 8 J cm^{-2}, which had a temperature of 871 K. However, the copper cube's temperature was only 617 K under the same conditions. When the side length of the copper cube was 90 nm, the temperature abruptly increased to 1520 K under 8 J cm^{-2} laser irradiation, which is approximately two times that at 4 J cm^{-2} (880 K). The reasons for the temperature response to laser fluence and edge-length between copper and aluminum could be attributed to their different melting points. The lower laser fluence can lead to an aluminum temperature of up to 890 K, and this temperature is far from the melting point of copper (1357.77 K). Additionally, aluminum is a type of active metal. Under laser irradiation, a series of collisions occur between

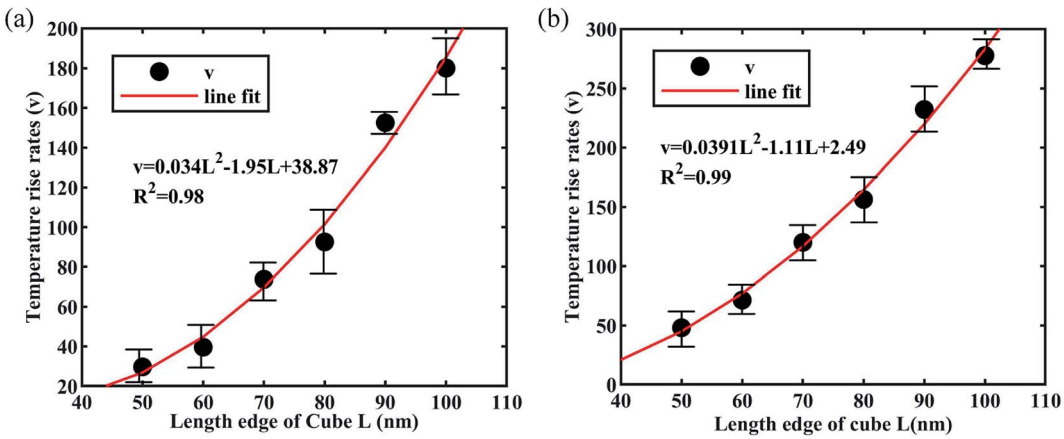

Fig. 7 Temperature rises rates with edge length of (a) copper and (b) aluminum cubes.

energetic particles and the lattice atoms of the metal. Aluminum can easily lose its electrons and be damaged by irradiation.

To validate the hypothesis that the rate of temperature rise is related to the edge length of the cubic impurities, we analyzed the average temperature rise rates (TRR). The TRR was calculated using the simulation. The growth curves for the relationship between the TRR and copper/aluminum cubes can be seen in Fig. 7(a) and (b). These graphs plot the TRR *vs.* cubes length (50–100 nm, 10 nm intervals). It can be seen from the graph that the TRR of the copper and aluminum cubes was similar, and that they could both take the form of a quadratic equation. However, as the laser fluence reached 8 J cm^{-2}, the temperature of the 100 nm aluminum cube was 2520 K, while that of copper was 1740 K, hence, the TRR of the aluminum cube was larger than that of the copper cube. The reasons were previously explained and are mainly determined by the characteristics of the material itself.

4. Conclusion

In this paper, we investigated a coupled model for electromagnetic radiation and heat conversion in a metal frame for laser-driven inertial confinement fusion. The process of reacting deuterium (D) and tritium (T) could generate a large amount of clean and recyclable energy, and the success of the laser ignition process relies on a clean optical system. The proposed coupled model can guide the choice of laser fluence, provide a method to improve the LIDT of materials in the system, and reduce impurities in the laser system. This work could provide an effective theoretical reference to control the nuclear reaction. On the basis of the simulation, the specific conclusions can be summarized as follows.

(1) The laser-induced damage threshold of the aluminum alloy could be improved by coating with a SiO_2 thin film. The light intensity enhancement factor of Al_2O_3 thin films could be significantly reduced after surface treatment.

(2) The existence of metal impurities in the aluminum alloy could result in melting of the metal frame and may cause impurity contamination of the laser system. Furthermore, the contaminated-environment will reduce the efficiency of laser transmission and would eventually lead to a failure of ignition; hence, further research on the metal impurities in the aluminum alloy frame is important.

(3) The temperature growth of the aluminum alloy is related to the edge length of the metal cube. At the nanoscale (<100 nm), the temperature growth for a cube of a certain length was found to be linear with increasing laser fluence. With increasing cube length, the growth rate of the temperature was larger.

In this work, a coupled model was built to verify the laser induced damage threshold of an aluminum alloy frame before and after being coated with SiO_2, and the results demonstrate the effect of nanoscale metal impurities on the temperature rise of the frame. It was shown that while metal impurities in the aluminum alloy frame were inevitable, surface treatment could provide effective protection and gives direction for the future design of such systems.

Nomenclatures

$^2_1$D	Deuterium
$\boldsymbol{H}$	Magnetic field
$^2_1$T	Tritium
r	Transmission coefficient
$^2_1$He	Helium
n_1	Refractive index of air
^{0}n	Neutron
n_2	Refractive index of materials
$^6_3$Li	Lithium
$\boldsymbol{E}_t$	Electric field under transmission wave of materials
P	Power dissipated
$\boldsymbol{E}_0$	Normalized electric field
$\boldsymbol{J}$	Current density
I	Light intensity value
$\boldsymbol{E}$	Electric field
S	Poynting vector
Q	Heat energy transfer rate (W m^{-3})
μ	Magnetic permeability
ω_0	Angular frequency
T	Temperature
ε	Permittivity
Φ	Laser fluence (J cm^{-2})

Conflicts of interest

There are no conflicts to declare.

Acknowledgements

This work was supported by the National Key Research and Development Program of China (No. 2017YFA0701200), the State Key Program of National Natural Science Foundation of China (No. 51535003), the State Key Laboratory of Precision Measurement Technology and Instruments (No. PILAB1701).

References

1 J. Meyer-Ter-Vehn, S. Atzeni and R. Ramis, *Rev. Sci. Instrum.*, 2010, **81**, 10E531.
2 H. Jie, K. Xiang-Shan, S. Jingjing, Y. Yu-Wei, W. Xuebang, C. S. Liu and S. Jun, *Nucl. Fusion*, 2018, **58**, 096021.
3 B. M. V. Wonterghem, C. A. Haynam, C. C. Widmayer, C. D. Marshall, C. D. Orth, E. Moses, G. M. Heestand, G. V. Erbert, J. Menapace and J. M. Auerbach, *Appl. Opt.*, 2007, **46**, 3276.
4 E. I. Moses, *Energy Convers. Manage.*, 2008, **49**, 1795–1802.
5 E. I. Moses and T. N. Collaborators, *Nucl. Fusion*, 2013, **53**, 104020.
6 C. J. Stolz, *Philos. Trans. R. Soc., A*, 2011, **370**, 4115–4129.
7 M. L. André, *Fusion Eng. Des.*, 1999, **44**, 43–49.
8 W. J. Hogan, E. I. Moses, B. E. Warner, M. S. Sorem and J. M. Soures, *Nucl. Fusion*, 2001, **43**, 567–573.
9 A. Rudenko, J. P. Colombier, S. Höhm, A. Rosenfeld, J. Krüger, J. Bonse and T. E. Itina, *Sci. Rep.*, 2017, **7**, 12306.

10 M. J. Chen, J. Cheng, X. D. Yuan, W. Liao, H. J. Wang, J. H. Wang, Y. Xiao and M. Q. Li, *Sci. Rep.*, 2015, **5**, 14422.
11 J. U. Kim, S. Lee, S. J. Kang and T. I. Kim, *Nanoscale*, 2018, **10**, 21555–21574.
12 M. ElKabbash, A. Sousa-Castillo, Q. Nguyen, R. Mariño-Fernández, N. Hoffman, M. A. Correa-Duarte and G. Strangi, *Adv. Opt. Mater.*, 2017, **5**, 1700617.
13 P. Singh and N. M. Ravindra, *Sol. Energy Mater. Sol. Cells*, 2012, **101**, 36–45.
14 M. Theelen, A. Liakopoulou, V. Hans, F. Daume, H. Steijvers, N. Barreau, Z. Vroon and M. Zeman, *J. Renewable Sustainable Energy*, 2017, **9**, 021205.
15 B. Stuart, M. Feit, A. Rubenchik, B. Shore and M. Perry, *Phys. Rev. Lett.*, 1995, **74**, 2248.
16 N. Shen, J. D. Bude and C. W. Carr, *Opt. Express*, 2014, **22**, 3393–3404.
17 M. Mahdieh and M. Gharibzadeh, *Opt. Laser Technol.*, 2012, **44**, 1713–1721.
18 N. S. Shcheblanov and T. E. Itina, *Appl. Phys. A: Mater. Sci. Process.*, 2013, **110**, 579–583.
19 P. Ge, C. Jiaxuan, L. Lihua, M. Xinxiang, D. Zhe and L. Daming, *Aerosol Sci. Technol.*, 2020, **54**, 342–352.
20 R. A. Negres, M. A. Norton, D. A. Cross and C. W. Carr, *Opt. Express*, 2010, **18**, 19966–19976.
21 H. Wan-Qing, H. Wei, W. Fang, X. Yong, L. Fu-Quan, F. Bin, J. Feng, W. Xiao-Feng, Z. Wan-Guo and Z. Xiao-Min, *Chin. Phys. Lett.*, 2009, **26**, 017901.
22 X. Cheng, J. Zhang, T. Ding, Z. Wei, H. Li and Z. Wang, *Light: Sci. Appl.*, 2013, **2**, e80.
23 Q. Bai, Y. Li, R. Shen, K. Zhang, X. Miao and F. Zhang, Molecular simulation and ablation property on the laser-induced metal surface, *SPIE Proceedings Vol. 11063: Pacific Rim Laser Damage 2019: Optical Materials for High-Power Lasers*, 2019, DOI: 10.1117/12.2539865.
24 G. C. Bhar, A. K. Chaudhary and P. Kumbhakar, *Appl. Surf. Sci.*, 2000, **161**, 155–162.
25 A. S. S. Kumar, N. Kishore, C. Mukherjee, R. Kamparath and S. Thakur, *Indian J. Phys.*, 2020, **94**, 105–115.
26 J. Cheng, M. Chen, K. Kafka, D. Austin, J. Wang, Y. Xiao and E. Chowdhury, *AIP Adv.*, 2016, **6**, 2248.
27 C. M. Brenner, A. Robinson, K. Markey, R. Scott, R. Gray, M. Rosinski, O. Deppert, J. Badziak, D. Batani and J. Davies, *Appl. Phys. Lett.*, 2014, **104**, 081123.
28 S. Vanalakar, G. Agawane, S. W. Shin, M. Suryawanshi, K. Gurav, K. Jeon, P. Patil, C. Jeong, J. Kim and J. Kim, *J. Alloys Compd.*, 2015, **619**, 109–121.
29 M. Han, W. Chen, H. Guo, L. Yu, B. Li and J. Jia, *J. Power Sources*, 2016, **318**, 121–127.
30 K. Moriya, K. Tanaka and H. Uchiki, *Jpn. J. Appl. Phys.*, 2007, **46**, 5780.
31 X. Zhang, W. Lin, J. Zheng, Y. Sun, B. Xia, L. Yan and B. Jiang, *J. Phys. Chem. C*, 2018, **122**, 596–603.
32 X. Liu, X. Lu, P. Wen, X. Shu and F. Chi, *Appl. Surf. Sci.*, 2017, **420**, 180–185.
33 H. H. Lim and T. Taira, *Opt. Express*, 2017, **25**, 6302–6310.
34 L. Lamaignère, R. Diaz, M. Chambonneau, P. Grua, J.-Y. Natoli and J.-L. Rullier, *J. Appl. Phys.*, 2017, **121**, 045306.
35 M. Chambonneau, J.-L. Rullier, P. Grua and L. Lamaignère, *Opt. Express*, 2018, **26**, 21819–21830.
36 F. Chi, N. Pan, C. Ding, X. Wang, F. Yi, X. Li and J. Lei, *Appl. Surf. Sci.*, 2019, **463**, 566–572.
37 A. O. Govorov and H. H. Richardson, *Nano Today*, 2007, **2**, 30–38.
38 G. Baffou, R. Quidant and F. J. García de Abajo, *ACS Nano*, 2010, **4**, 709–716.

